J. Fluid Mech. (1987), *vol.* 181, *pp.* 197–212
Printed in Great Britain

Transient cavities near boundaries Part 2. Free surface

By J. R. BLAKE, B. B. TAIB† AND G. DOHERTY
Department of Mathematics, The University of Wollongong, Wollongong, New South Wales, 2500 Australia

(Received 21 February 1986 and in revised form 15 January 1987)

Calculations of the growth and collapse of transient vapour cavities near a free surface when buoyancy forces may be important are made using the boundary-integral method described in Part 1. Bubble shapes, particle paths, pressure contours and centroid motion are used to illustrate the calculations. In the absence of buoyancy forces the bubble migrates away from the free surface during the collapse phase, yielding a liquid jet directed away from the free surface. When the bubble is sufficiently close to the free surface, the nonlinear response of the free surface produces a high-speed jet ('spike') that moves in the opposite direction to the liquid jet and, in so doing, produces a stagnation point in the fluid between the bubble and the free surface. For sufficiently large bubbles, buoyancy forces may be dominant, so that the bubble migrates towards the free surface with the resulting liquid jet in the same direction. The Kelvin impulse provides a reasonable estimate of the physical parameter space that determines the migratory behaviour of the collapsing bubbles.

1. Introduction

The interaction between a pulsating bubble and a free surface was first studied in the case of underwater explosions, the main concern being the influence of the free surface on the direction of motion of the bubble and the period of oscillation (see for example Holt 1977). Experimental observations reported in Gibson (1968), Chahine (1977), Gibson & Blake (1980), Blake & Gibson (1981), and theoretical and numerical calculations reported in Blake & Gibson (1981), Blake & Cerone (1982), Blake (1983), and Cerone & Blake (1984) showed that the bubble motion and the jet formed during the bubble collapse are directed *away* from a free surface in contrast to the case of a bubble collapsing near a rigid boundary when the bubble motion and the jet are directed *towards* the boundary.

To facilitate the use of high-speed cameras in experimental studies of vapour-bubble dynamics, the lifetime of the bubble is increased by reducing the ambient fluid pressure, resulting in relatively large bubbles for which buoyancy forces might become important. Using this technique, Chahine & Bovis (1980), observed two different directions of motion of a cavitation bubble beneath a two-liquid interface (with the bubble located in the denser liquid). The bubble migrated away from the interface when closer than a certain critical distance and moved towards it if further away. The case when the bubble moves towards the interface may be due to buoyancy forces, as our numerical calculations and the theoretical calculation of Blake & Cerone

† Current address: Mathematics Department, Universiti Pertanian Malaysia, Serdang, Selangor, Malaysia.

(1982) suggest that, without buoyancy forces, the bubble should always move away from the less-dense fluid.

While the rigid boundary may be regarded as the infinite-inertia limit for a boundary, a free surface is the exact opposite being the zero-inertia limit. Thus we might expect that, near a deformable boundary, the bubble response might lie somewhere between these two extremes.

In a recent paper Gibson & Blake (1982) suggested that a suitable deformable, yet resilient, material might be used to coat rigid hydraulic structures to reduce, or even eliminate, cavitation damage. In a companion paper Blake, Taib & Doherty (1986, hereinafter referred to as Part 1) consider the motion of a cavitation bubble near a rigid boundary in the presence of buoyancy forces and an incident stagnation-point flow. While we cannot include stagnation-point flow in this study of the free surface we can readily include buoyancy forces and thus compare and contrast the response of the bubble near a free surface with that near a rigid boundary.

In this paper we apply the boundary-integral method developed in Taib, Doherty & Blake (1984) to the study of buoyant vapour cavities near a free surface. Calculations yield details of the bubble and free-surface shape, particle pathlines, centroid motion and contours of the pressure field. This numerical study appears to be of significantly higher accuracy than earlier studies of the free-surface problem by Lenoir (1976), Blake & Gibson (1981), Cerone & Blake (1984) and Blake, Cerone & Gibson (1984). In our study the computations are usually terminated when the high-speed jet is about to pierce the free surface on the other side of the bubble. A brief discussion of the numerical techniques employed in the free-surface calculations may also be found in §2, although a more extensive discussion may be found in Part 1 and in Taib *et al.* (1984). Results of the calculations for bubble shapes, particle pathlines, centroid motion and pressure contours are shown in §3.

Following the ideas developed for the Kelvin impulse in Part 1 we are able to extend the calculations for the critical parameters that were initially developed in the report by Blake *et al.* (1984). With the following parameters defined:

$$\beta = \gamma\delta, \quad \gamma = \frac{h}{R_{\mathrm{m}}}, \quad \delta = \pm\left(\frac{\rho g R_{\mathrm{m}}}{\Delta p}\right)^{\frac{1}{2}}, \tag{1}$$

where h is the distance of the bubble centroid from the free surface initially, R_{m} is the maximum bubble radius, ρ the density, g gravitational acceleration and Δp is the difference between the ambient pressure at the centroid, in the absence of the bubble, and the vapour pressure, they showed that the magnitude of β determined the sign of the Kelvin impulse and hence the direction of migration and subsequent jet formation in the cavitation bubble. Experimental, analytical and numerical studies appear to confirm that the critical value of β lies around 0.5. A modification of their calculations is presented in §4 yielding a smaller critical value of β but with some modifications near $\gamma \approx 1.0$.

In the concluding section the present results are summarized and compared with the previously obtained results for a rigid boundary that were present in Part 1.

2. Theory and numerical analysis

In this section supplementary theory to that presented in Part 1 is developed to model the growth and collapse of an axisymmetric cavitation bubble near a free surface while the bubble is subject to buoyancy forces. Buoyancy forces are typically unimportant in cavitation but are of the utmost importance in underwater explosions.

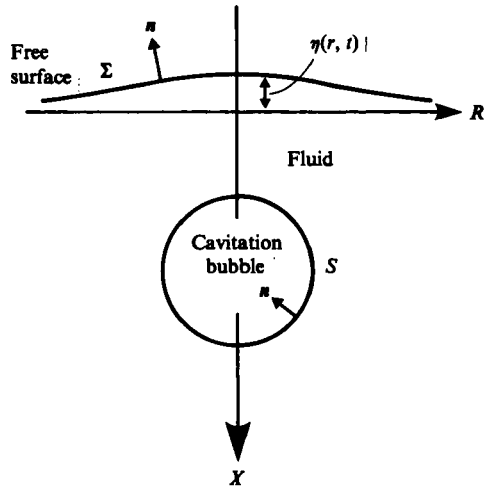

FIGURE 1. Geometry used to model the growth and collapse of a vapour bubble near a free surface.

Buoyancy forces also allow the introduction of a pressure gradient into the dynamics of bubble motion without an associated ambient-fluid motion. Details of the geometry may be found in figure 1.

As in Part 1 we assume that the fluid motion is incompressible, inviscid and irrotational with the action of surface tension being neglected on both the bubble and free surface. Thus we may represent the velocity as the gradient of a potential which satisfies Laplace's equation as follows:

$$\boldsymbol{u} = \nabla\phi, \quad \nabla^2\phi = 0, \tag{2}$$

where $\boldsymbol{u}$ is the Cartesian velocity vector and ϕ is the potential.

Initially the cavitation bubble is taken to be a sphere of 'small' radius R_0 whose centre is located a distance h below the free surface. The initial potential on the bubble surface at time t_0 is obtained from the Rayleigh bubble solution ϕ_0^{R} appropriately modified for the presence of the flat free surface by incorporating the negative image as follows:

$$\phi_0 = \phi_0^{\mathrm{R}}\left(1 - \frac{R_0}{[(x+h)^2+r^2]^{\frac{1}{2}}}\right), \tag{3a}$$

where

$$\phi_0^{\mathrm{R}}(R_0, t_\epsilon) = -R_0\left[\frac{2}{3}\left(\frac{\Delta p}{\rho}\right)\left\{\frac{R_{\mathrm{m}}^3}{R_0^3} - 1\right\}\right]^{\frac{1}{2}}, \tag{3b}$$

where t_ϵ is the initial time which can be expressed in terms of an incomplete beta function

$$t_\epsilon = 3\left(\frac{3\rho}{2\Delta p}\right)^{\frac{1}{2}} B_a\left(\tfrac{5}{6}, \tfrac{3}{2}\right), \quad a = \left(\frac{R_0}{R_m}\right)^3. \tag{3c}$$

Here Δp is the difference in pressure between the initial static pressure at h and the vapour pressure p_{c} (i.e. $\Delta p = p_0 + \rho g h - p_{\mathrm{c}}$), ρ is the density, while x and r are the axial and radial cylindrical polar coordinates respectively. The potential on the initially flat free surface is taken to be zero as would occur in the linear theory. At

large distances from the bubble, the velocity tends to zero while the pressure approaches the static pressure field, i.e.

$$\boldsymbol{u} \to 0, \quad p \to p_0 + \rho g x, \tag{4}$$

where p_0 is the constant pressure on the free surface.

As the fluid particles remain on the bubble surface and free surface, we may take these 'particle velocities' to be the fluid velocity as follows:

$$\frac{\mathrm{d}\boldsymbol{x}}{\mathrm{d}t} = [\nabla\phi]. \tag{5}$$

That is, we are using a Lagrangian description for the surface particles to specify the shape of the bubble and the free surface. The dynamic condition on the bubble surface is obtained by equating the dynamic pressure to the vapour pressure,

$$p_c = p_0 + \rho g x - \rho \frac{\partial \phi}{\partial t} - \tfrac{1}{2}\rho |\boldsymbol{u}|^2, \tag{6}$$

while on the free surface it is equated to the constant pressure p_0,

$$p_0 = p_0 + \rho g x - \rho \frac{\partial \phi}{\partial t} - \tfrac{1}{2}\rho |\boldsymbol{u}|^2. \tag{7}$$

Before developing the numerical solutions it proves convenient to scale all terms in the equations to make them dimensionless and to yield the dimensionless groups of (1). Lengths are scaled with respect to the maximum bubble radius:

$$X = \frac{x}{R_m}, \quad R = \frac{r}{R_m}. \tag{8}$$

Quantities involving time explicitly or implicitly are scaled with respect to

$$T^* = \frac{R_m}{[\Delta p/\rho]^{\frac{1}{2}}}. \tag{9}$$

The dimensionless pressure field P is defined as

$$P = \frac{p - p_c}{p_0 + \rho g h - p_c}. \tag{10}$$

Equations (6) and (7) may be rearranged and scaled to yield $\partial\phi/\partial t$ for the bubble

$$\frac{\partial \phi}{\partial t} = 1 - \tfrac{1}{2}|\boldsymbol{u}|^2 + \delta^2(X - \gamma), \tag{11a}$$

and for the free surface

$$\frac{\partial \phi}{\partial t} = -\tfrac{1}{2}|\boldsymbol{u}|^2 + \delta^2 X. \tag{11b}$$

Physically δ corresponds to the ratio of the half-lifetime of the bubble to the time it takes a bubble of radius R_m to rise one radius from rest due to buoyancy forces.

The above equations are solved by using a boundary-integral method, as outlined in Taib *et al.* (1984) and in Part 1. The appropriate formulation is as follows,

$$c\phi = \int_{S \cup \Sigma} \left(\frac{\partial \phi}{\partial n} G - \phi \frac{\partial G}{\partial n} \right) \mathrm{d}S, \tag{12}$$

where ϕ is the potential, $\partial\phi/\partial n$ the normal velocity with $\boldsymbol{n}$ the outward normal, S the bubble surface and Σ the free surface (see figure 1). The coefficient c takes the

value 2π if a point lies on either the bubble or the free surface and 4π if it is in the domain of the fluid. The Green function G that is used in this study is that due to a source in an infinite fluid, in contrast to Part 1 which also includes the image source to balance the zero normal velocity on the surface of the rigid boundary. Because of axisymmetry the Green function may be integrated through the azimuthal angle to yield an expression containing complete elliptic integrals.

The surface of the bubble and the free surface are specified by $N+1$ and $M+1$ Lagrangian points respectively. This leads to N and M segments on which x, r, ϕ and $\partial\phi/\partial n$ need to be specified by a linear isoparametric approximation.

As the initial bubble shape and the potential are specified, the appropriate strategy is to solve (12) for the normal velocity $\partial\phi/\partial n$. This, together with the tangential velocity, enables us to calculate the velocity of all the specified points on both the surface of the bubble and free surface, and hence update their position and potential using the following relations:

$$\left.\begin{aligned} x_j(t+\Delta t) &= x_j(t)+u_j\,\Delta t+O(\Delta t)^2,\\ r_j(t+\Delta t) &= r_j(t)+v_j\,\Delta t+O(\Delta t)^2,\\ \phi_j(t+\Delta t) &= \phi_j(t)+\left(\frac{\partial\phi}{\partial t}+|\boldsymbol{u}|^2\right)_j\Delta t+O(\Delta t)^2. \end{aligned}\right\} \tag{13}$$

The values for $\partial\phi/\partial t$ may be obtained from (11a, b) noting that they are different for the bubble and the free surface. This procedure is repeated until the bubble has collapsed, thus yielding a time history of the bubble shape and particle paths and also allowing the calculation of the pressure field and instantaneous streamlines at specially chosen times. In the next section our calculations are illustrated in graphical form. Further details of the numerical-analysis procedures may be found in Part 1 and Taib *et al.* (1984).

For values of γ near 1 the free surface developed a saw-toothed-like profile close to the axis of symmetry when the cavitation bubble was near maximum size. This instability was removed by using the five-point smoothing formula of Longuet-Higgins & Cokelet (1976). The smoothing formula was applied after every five time-steps.

3. Computational results

In this section we illustrate bubble and free-surface shapes, particle paths, centroid motion and pressure contours for a vapour bubble near a free surface with and also without buoyancy forces affecting the fluid motion. Experimentally, this latter state is achieved by conducting the experiments in a falling rig. In the calculations N and M are equal to either 16 or 32. Computations were performed on the UNIVAC 1100/60 computer at the University of Wollongong Computer Centre.

3.1. *Buoyancy forces omitted*

The bubble and free-surface shape at selected dimensionless times T are shown in figures 2 and 3 for $\gamma = 1.5$ and 1.0 respectively. In contrast to the rigid-boundary case, the lifetime of the bubble is shortened when the growth begins nearer to the free surface (smaller value of γ).

During the growth phase in the $\gamma = 1.5$ example the bubble grows almost spherically. The free surface is pushed up by the growth of the bubble. During the

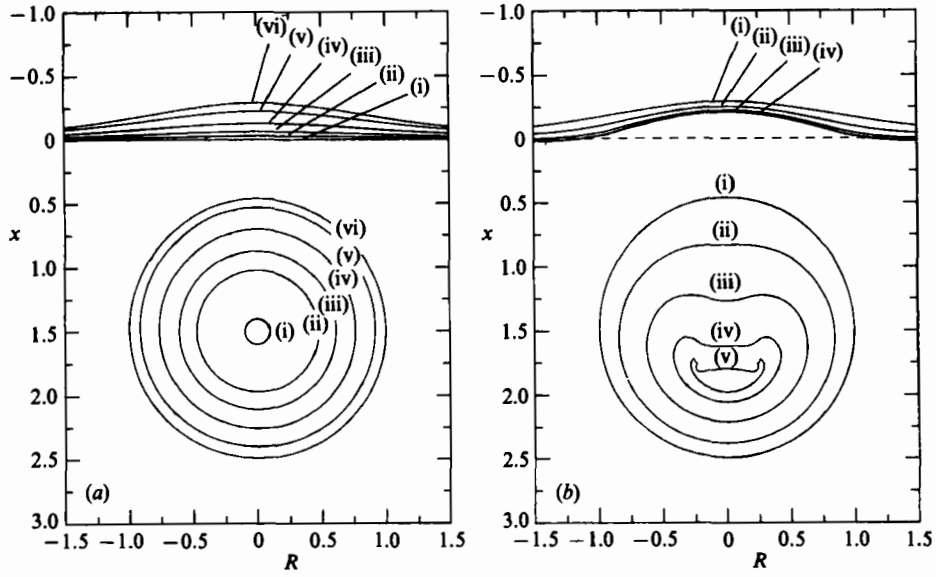

FIGURE 2. Bubble and free-surface shapes for $\gamma = 1.5$ during (*a*) expansion phase at dimensionless times (i) 0.0016, (ii) 0.136, (iii) 0.252, (iv) 0.452, (v) 0.668, (vi) 0.777, and (*b*) collapse phase at dimensionless times (i) 0.777, (ii) 1.252, (iii) 1.449, (iv) 1.547, and (v) 1.577.

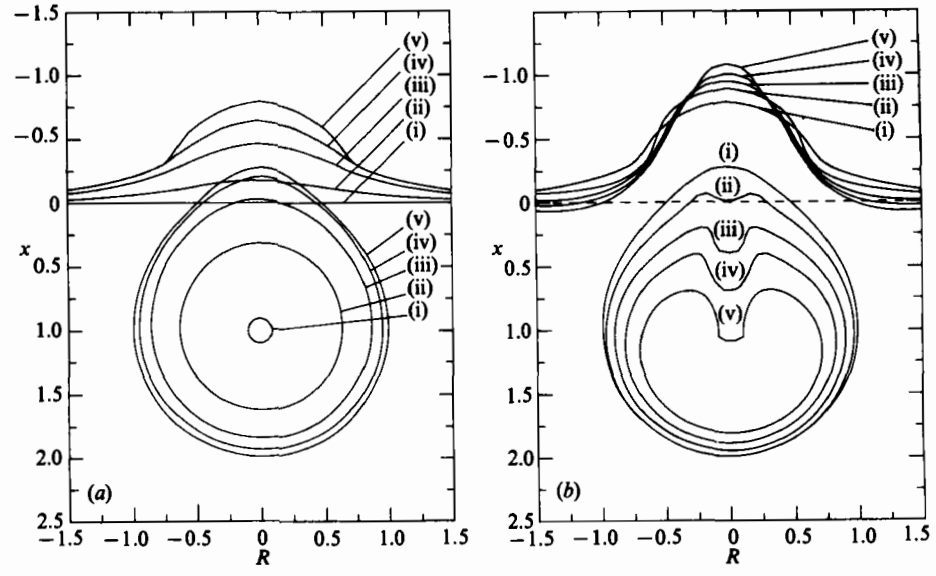

FIGURE 3. Bubble and free-surface shape for $\gamma = 1.0$ during (*a*) expansion phase at dimensionless times (i) 0.0016, (ii) 0.149, (iii) 0.356, (iv) 0.506, (v) 0.706, and (*b*) collapse phase at dimensionless times (i) 0.706, (ii) 0.930, (iii) 1.084, (iv) 1.186, (v) 1.310.

collapse phase the free surface 'falls' with the collapse of the bubble. However the rate of 'fall' of the points near the axis of symmetry on the free surface is slightly slower than the rest of the points surrounding them resulting in a pronounced free-surface hump at the conclusion of the collapse phase. As the collapse progresses the surface of the bubble nearer to the free surface becomes flattened and forms a

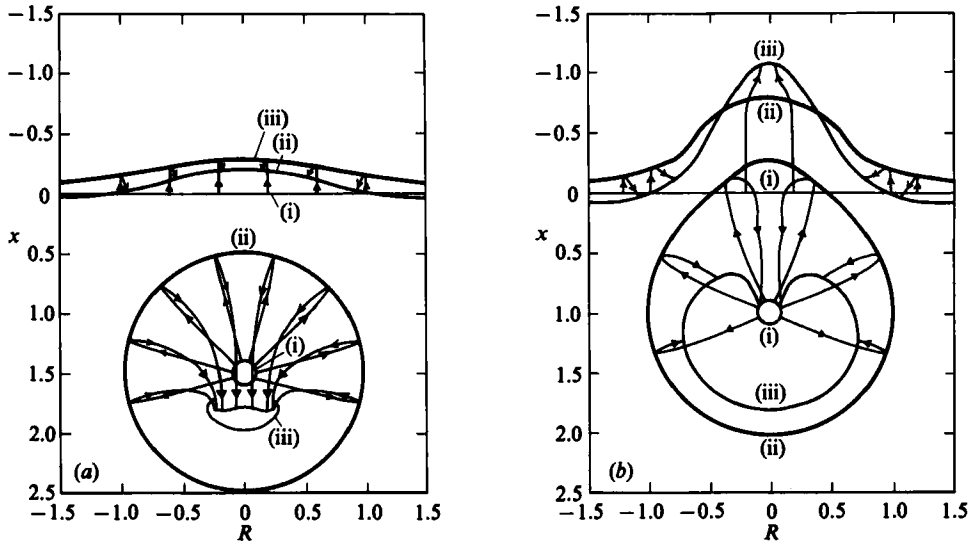

FIGURE 4. Pathlines of selected fluid particles on the bubble and free surface for the cases (*a*) $\gamma = 1.5$ and (*b*) 1.0. The bubbles and free surfaces shown are (i) initial, (ii) maximum volume and (iii) the final shape.

jet directed away from the free surface. The jet is much broader than those in the rigid-boundary case.

In the second example ($\gamma = 1.0$), the surface of the bubble nearer to the free surface (top of the bubble) moves towards the free surface and is elongated in this direction, causing a substantial free-surface hump. As the expansion phase progresses, the top of the bubble is entrained into the base of the raised free surface. During the collapse phase the bubble migrates away from the free surface while the free-surface hump or 'spike' continues to grow along the axis of symmetry. Therefore, the free surface and the adjacent bubble surface are moving in opposite directions producing a stagnation point on the axis of symmetry between the two surfaces. Instantaneous streamlines clearly showing the stagnation point may be found in Cerone & Blake (1984) while velocity vectors are plotted in Taib (1985) to illustrate the phenomenon. The nonlinear interaction between the free surface and the bubble will be discussed further when we consider the pressure contours.

Figure 4 shows the pathlines of selected particles on both the bubble and free surface together with three shapes of bubble and free surface, the initial, the maximum volume and the final for $\gamma = 1.5$ and $\gamma = 1.0$. On the bubble surface, the particles move almost radially during the growth phase. However, during the collapse phase, the particles 'loop' around with an initially inward radial motion before being swept into the liquid jet where particles move almost parallel to the axis of symmetry. During the expansion phase the particles on the free surface move almost parallel to the axis of symmetry but during the collapse phase the particles migrate towards the axis of symmetry. For the case $\gamma = 1.0$, the particles near the axis of symmetry continue to move upwards towards the axis of symmetry, confirming that the free-surface hump or 'spike' and the liquid jet in the bubble are moving in opposite directions.

In figure 5, equispaced pressure contours are shown for the case of $\gamma = 1.0$. The dimensionless times in the two examples are (*a*) 1.186, (*b*) 1.310. The point of

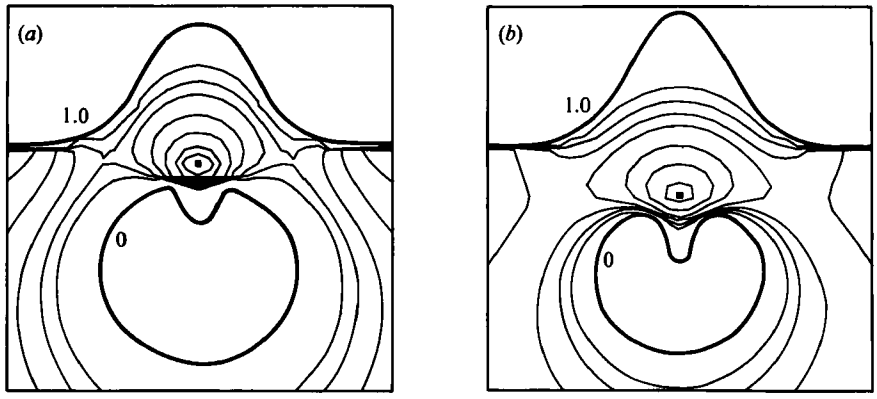

FIGURE 5. Equally spaced pressure contours for a vapour bubble near a free surface for the case $\gamma = 1.0$ at dimensionless times (*a*) 1.186 and (*b*) 1.310. A point of maximum pressure occurs on the axis of symmetry between the bubble and the free surface.

maximum pressure is located on the axis of symmetry between the bubble and the free surface. The location of the stagnation point and the point of maximum pressure do not coincide as they would in steady flow. Similar phenomena were also predicted by Cerone & Blake (1984). During the bubble collapse phase, fluid is drawn in towards the bubble from the region of least mass (i.e. the region which corresponds to the shortest distance between the bubble and the free surface). As the collapse continues, a point of maximum pressure is created on the axis of symmetry forcing the fluid to move in opposite directions and thus creating an instantaneous stagnation point (see also Cerone & Blake 1984).

Figures 6 and 7 compare the numerical and experimental bubble and free-surface shapes reported in Blake & Gibson (1981) for $\gamma = 1.68$ and 0.98 respectively. In the first case, $\gamma = 1.68$, the bubble and the free-surface shapes are in good agreement with the experimental observations of Blake & Gibson (1981) with the exception of the final bubble shape. In our model the jet is slightly broader than those observed experimentally. However, our final shape more closely resembles the bubble shape observed by Chahine (1977, see figure 9*a* for $\gamma = 1.67$).

In the second case, $\gamma = 0.98$, the bubble and the free-surface shape during the growth phase are in general agreement with the experimental observations. The key feature is that, during the latter stages of the expansion phase, the bubble is entrained into the raised free surface. However, during the collapse phase, the theoretical model predicts the formation of a narrow jet relatively early on. The broader jet observed in the experiments may be due to interference with the jet by the electrodes in the experimental apparatus. The numerical model breaks down before the collapse is concluded.

Figure 8 compares theory and experiment for the movement of the bubble centroid for $\gamma = 2.26$, 1.68 and 0.98. During the early expansion phase there is a slight movement of the centroid towards the free surface in both theory and experiment. The centroid begins to move away from the free surface before the expansion phase concludes and this movement increases rapidly during the collapse phase.

3.2. *Buoyancy forces included*

In figures 9 and 10 we illustrate the cases $\gamma = 1.8$ with $\delta = 0.15$ and 0.5 respectively (i.e. $\gamma\delta = 0.27$ and 0.9 respectively). In the first example (figure 9), at maximum

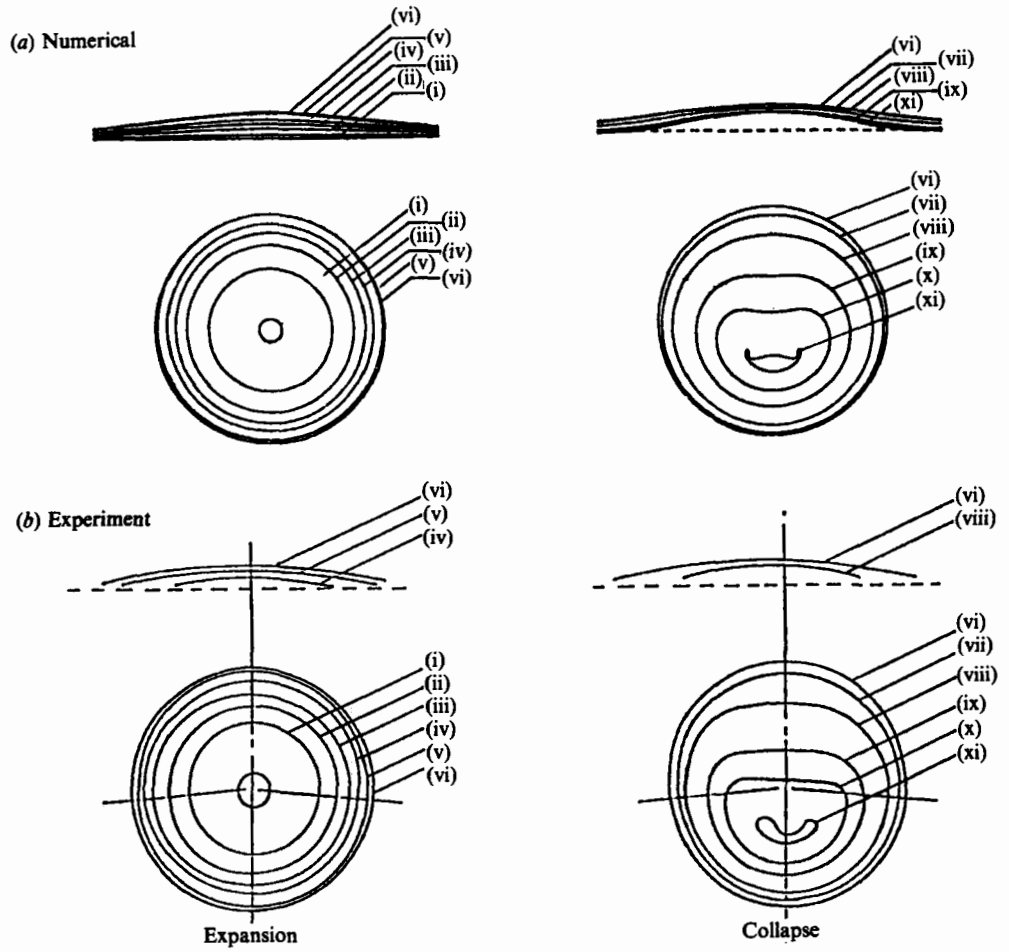

FIGURE 6. Comparison of numerical calculations with experiment (from Blake & Gibson 1981) for the growth and collapse of a vapour bubble near a free surface at $\gamma = 1.68$. Dimensionless times are (i) 0.102, (ii) 0.205, (iii) 0.307, (iv) 0.410, (v) 0.615, (vi) 0.820, (vii) 1.025, (viii) 1.230, (ix) 1.434, (x) 1.537, (xi) 1.609. (Note: time for numerical shape (xi) is 1.601.)

volume, the bubble is slightly elongated towards the free surface. The free surface collapses with the collapse of the bubble and the bubble migrates away from the free surface with the jet directed away from it. During the collapse phase, for the $\delta = 0.5$ case, the bubble migrates towards the free surface with the broad jet directed towards it.

We now consider the cases $\gamma = 1.24$ with $\delta = 0.2$ and 0.8 (i.e. $\gamma\delta = 0.248$ and 0.992 respectively). In the early expansion phase for the case when $\delta = 0.2$ (figure 11) the bubble grows almost spherically. However, near the maximum volume, the top portion of the bubble is attracted towards the free surface by becoming elongated towards it. During the collapse phase, the bubble is repelled by the free surface. The bubble forms a liquid jet directed away from the free surface. The jet is becoming broader as the collapse progresses.

In figure 12, with $\delta = 0.8$, the bubble is pushed nearer to the free surface. Physically this situation is unlikely to occur in the laboratory but may occur for large underwater explosion cavities. At maximum volume the top portion of the bubble

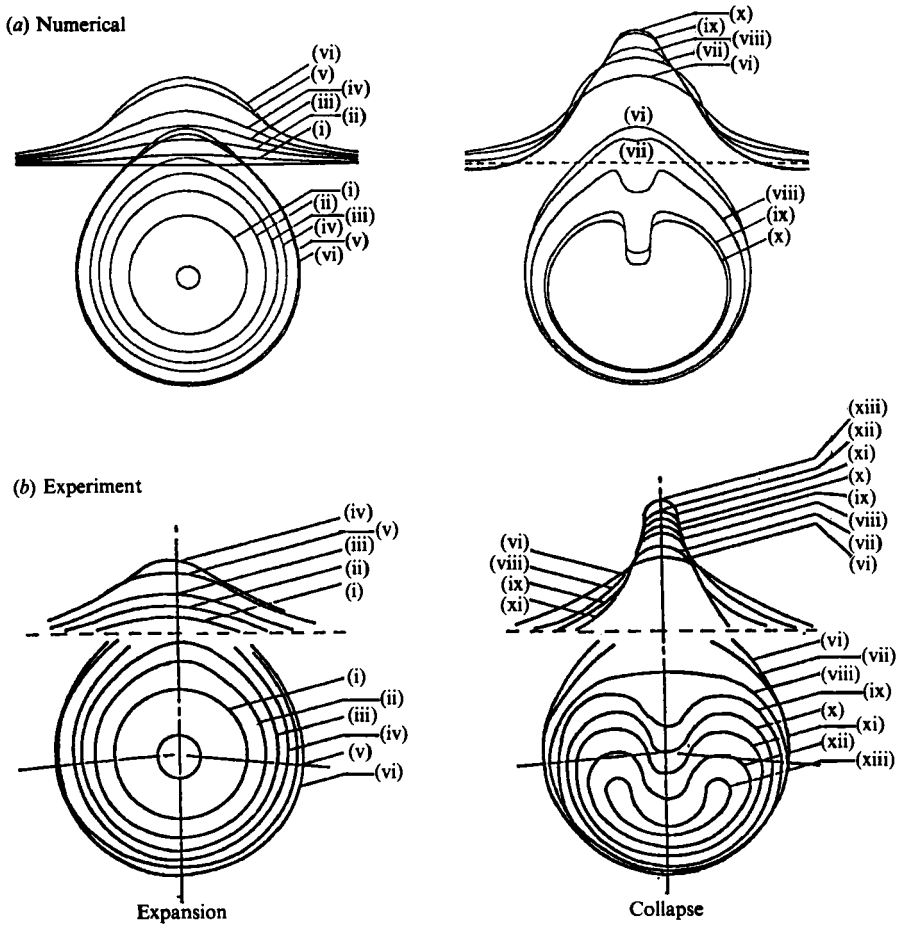

FIGURE 7. Comparison of numerical calculations with experiment (from Blake & Gibson 1981) for the growth and collapse of a vapour bubble near a free surface at $\gamma = 0.98$. Dimensionless times are (i) 0.087, (ii) 0.173, (iii) 0.260, (iv) 0.347, (v) 0.520, (vi) 0.604, (vii) 0.867, (viii) 1.040, (ix) 1.214, (x) 1.300, (xi) 1.387, (xii) 1.474, (xiii) 1.508. (Note: time for numerical shape (x) is 1.251.)

is entrained underneath the raised free surface. One would expect that during the collapse phase the free-surface hump would continue to grow. However, in this case, the free surface collapses with the collapse of the bubble. The physical explanation is that, as we shall see later, the maximum pressure no longer occurs between the bubble and the free surface, but at a point near the bottom of the bubble. As the collapse phase progresses, the bottom part of the bubble becomes flattened and forms a jet directed towards the free surface.

The equispaced pressure contours for the cases of $\gamma = 1.24$ with $\delta = 0.2$ and 0.8 are illustrated in figure 13(a, b) at the dimensionless times (a) 1.523, (b) 1.556. In figure 13(a), the point of maximum pressure is located on the axis of symmetry between the bubble and the free surface while in figure 13(b), the point of maximum pressure is located underneath the bubble (i.e. on the opposite side of the bubble to the free surface).

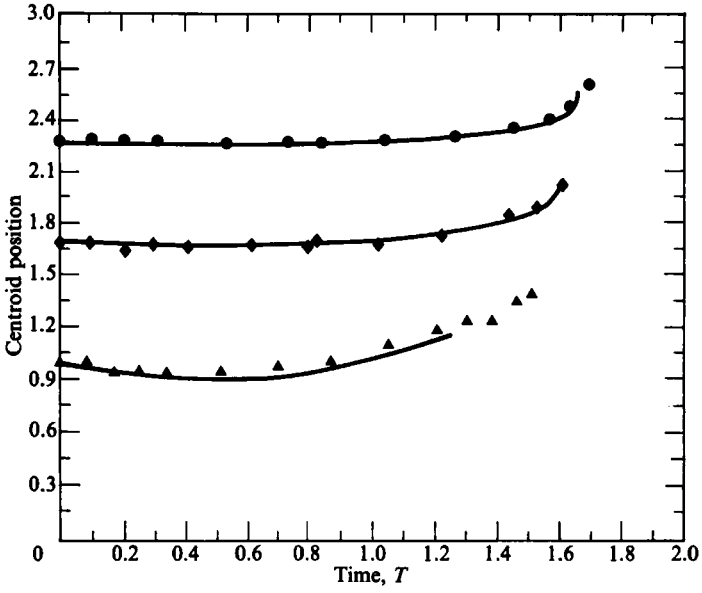

FIGURE 8. Comparison of numerical calculations (——) with experiment (▲, $\gamma = 0.98$; ◆, 1.68; ●, 2.26) (from Blake & Gibson 1981) for the movement of the bubble centroid during the growth and collapse of a vapour bubble near a free surface.

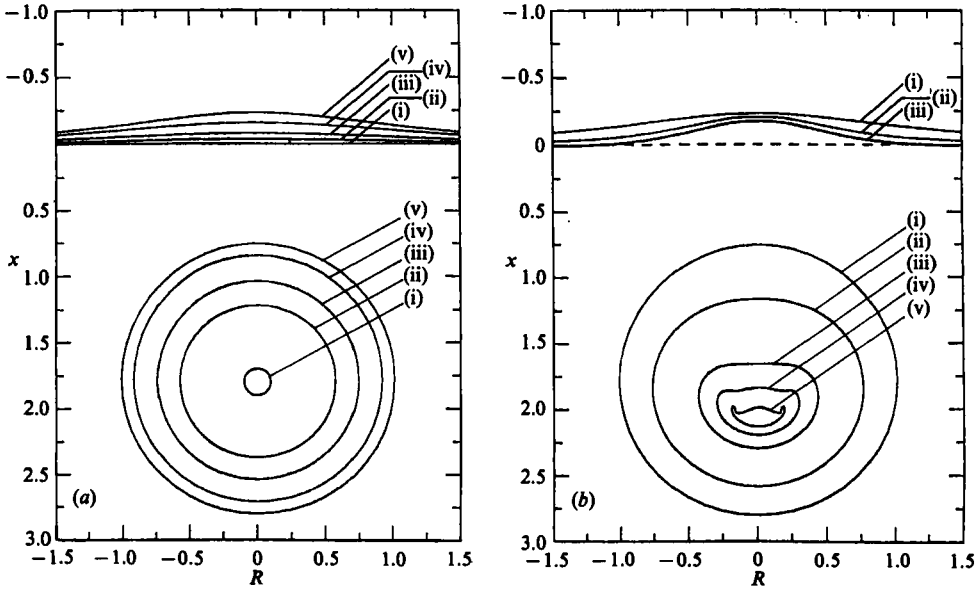

FIGURE 9. Bubble and free-surface shapes for $\gamma = 1.8$ and $\delta = 0.15$ ($\gamma\delta = 0.27$) during (*a*) expansion phase at dimensionless times (i) 0.0016, (ii) 0.117, (iii) 0.235, (iv) 0.459, (v) 0.666, and (*b*) collapse phase at dimensionless times (i) 0.666, (ii) 1.391, (iii) 1.585, (iv) 1.617, (v) 1.631.

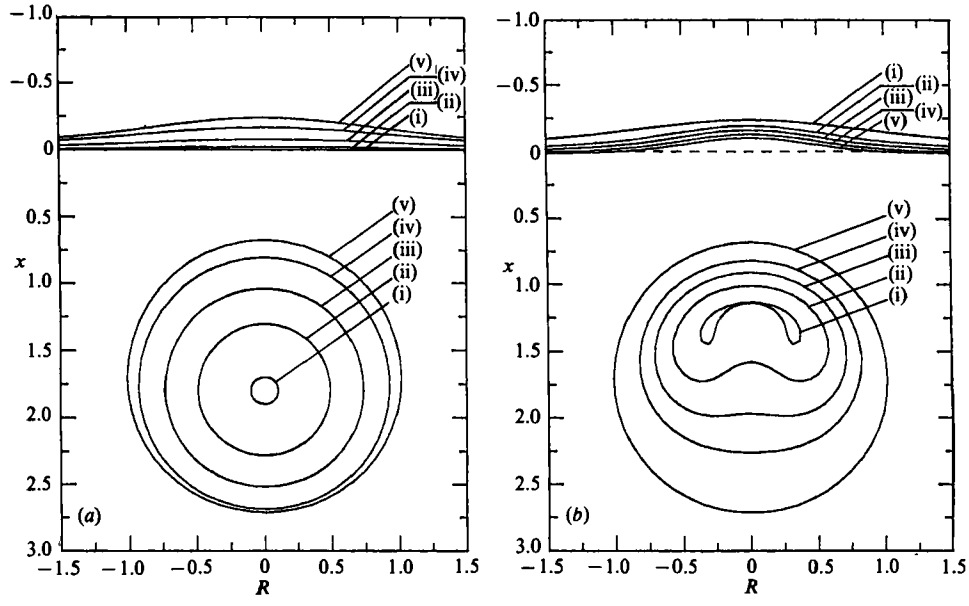

FIGURE 10. Bubble and free surface shapes for $\gamma = 1.8$ and $\delta = 0.5$ ($\gamma\delta = 0.9$) during (*a*) expansion phase at dimensionless times (i) 0.0016, (ii) 0.077, (iii) 0.227, (iv) 0.480, (v) 0.821, and (*b*) collapse phase at dimensionless times (i) 0.821, (ii) 1.360, (iii) 1.472, (iv) 1.564, (v) 1.645.

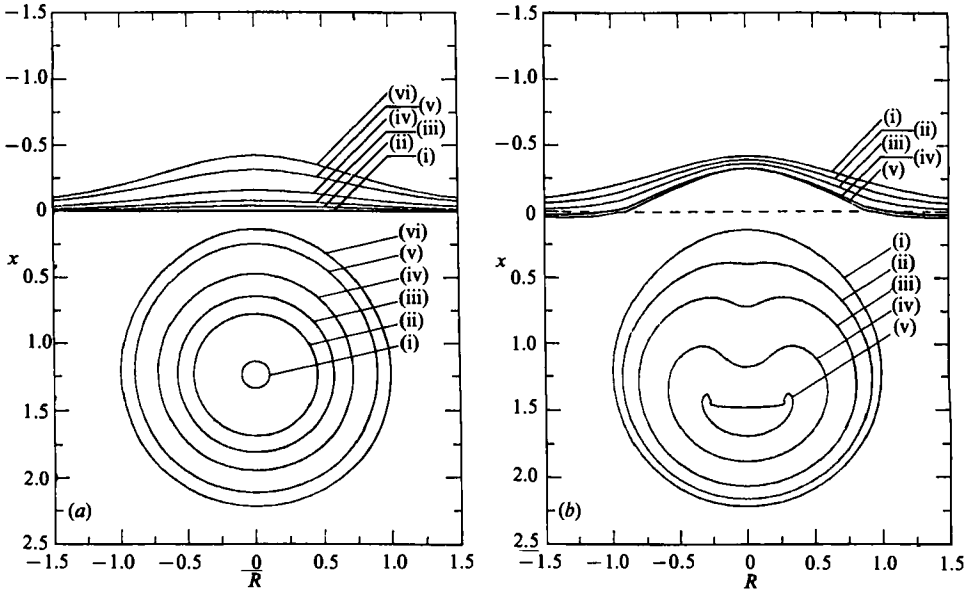

FIGURE 11. Bubble and free surface shapes for $\gamma = 1.24$ and $\delta = 0.2$ ($\gamma\delta = 0.248$) during (*a*) expansion phase at dimensionless times (i) 0.0016, (ii) 0.063, (iii) 0.115, (iv) 0.207, (v) 0.407, (vi) 0.757, and (*b*) collapse phase at dimensionless times (i) 0.757, (ii) 1.082, (iii) 1.254, (iv) 1.431, (v) 1.523.

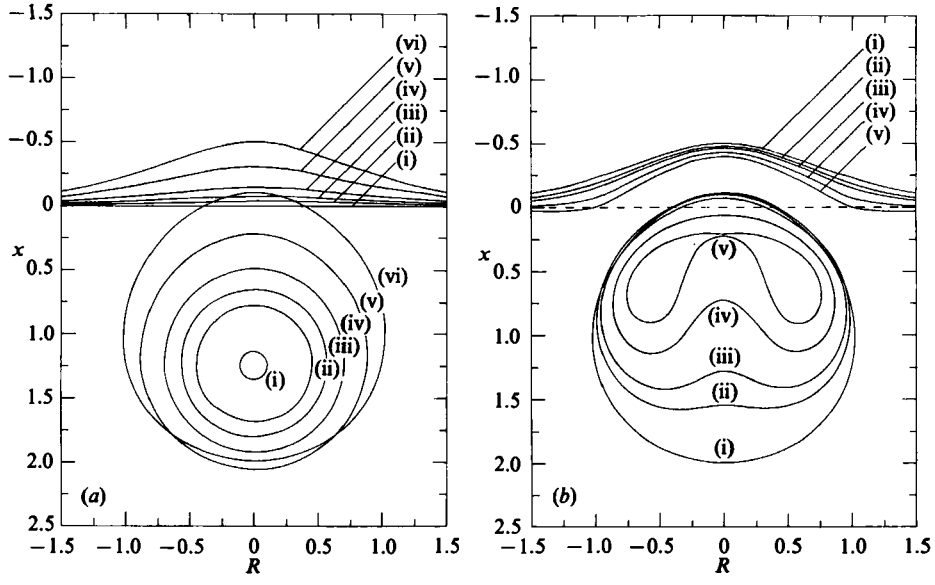

FIGURE 12. Bubble and free surface shapes for $\gamma = 1.24$ and $\delta = 0.8$ ($\gamma\delta = 0.992$) during (*a*) expansion phase at dimensionless times (i) 0.0016, (ii) 0.062, (iii) 0.111, (iv) 0.193, (v) 0.387, (vi) 0.812, and (*b*) collapse phase at dimensionless times (i) 0.812, (ii) 1.131, (iii) 1.230, (iv) 1.405, (v) 1.556.

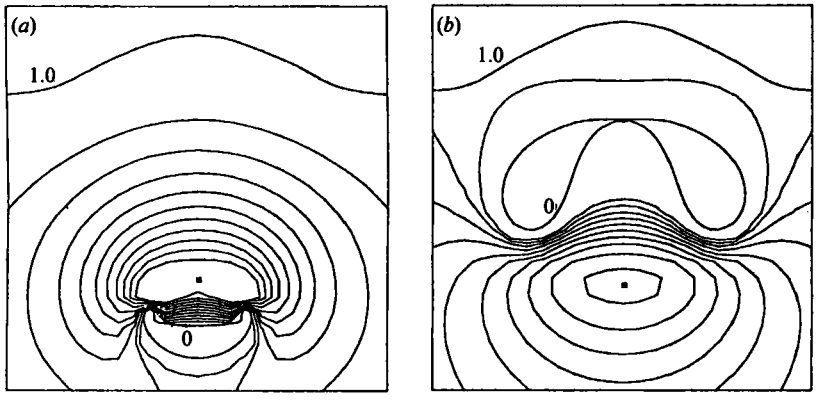

FIGURE 13. Equally spaced pressure contours for a vapour bubble near a free surface, for the case $\gamma = 1.24$ and (*a*) $\delta = 0.2$ at dimensionless time 1.523. A point of maximum pressure occurs on the axis of symmetry between the bubble and the free surface. (*b*) $\delta = 0.8$ at dimensionless time 1.556. A point of maximum pressure occurs on the axis of symmetry near the lower portion of the bubble.

4. Kelvin impulse

Following the ideas on the Kelvin impulse in Part 1, we may represent the growth and collapse phases of the cavitation bubble by a time-varying strength source $m(t)$. Thus, from Blake *et al.* (1984) we obtain the following expression for the x-component of the 'force' $\boldsymbol{F}$:

$$F_x(t) = -\rho g V(t) + \frac{\rho m^2}{16\pi h^2} - \frac{\rho g}{8\pi h^3} m \int_0^t (t-\tau)\, m(\tau)\, \mathrm{d}\tau + O\left(\frac{\rho m^2 t^4 g^2}{h^4}\right). \tag{14}$$

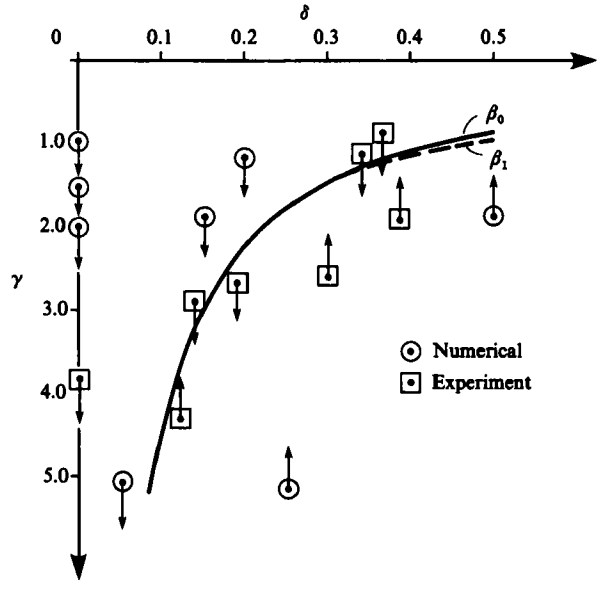

FIGURE 14. Graphical tabulation of numerical calculations and experimental studies conducted at different parameter values of γ and δ. The arrows indicate direction of jet and bubble migration. The null-Kelvin-impulse lines corresponding to $\beta_0 = \gamma\delta = 0.442$ and β_1, which is the solution of (16b), are shown on the diagram.

The Kelvin impulse at the completion of the bubble collapse is

$$I_x(T_c) = \int_0^{T_c} F_x(t)\,\mathrm{d}t, \tag{15a}$$

which yields, upon integration, for large γ

$$I_x(T_c) = \frac{\pi R_m^5 (\frac{2}{3})^{\frac{3}{2}} (\rho\Delta p)^{\frac{1}{2}}}{h^2}\left[B(\tfrac{7}{6},\tfrac{3}{2}) - 2\gamma^2\delta^2 B(\tfrac{11}{6},\tfrac{1}{2}) + \frac{1}{3}\frac{\delta^2}{\gamma}B(\tfrac{17}{6},\tfrac{1}{2}) + O\left(\frac{1}{\gamma^3}\right)\right], \tag{15b}$$

where $B(x, y)$ is a beta function.

The null-impulse curve for the two parameters (γ, δ) may be obtained by equating $I_x(T_c)$ to zero. For large γ we may equate either the first two or first three terms in (15b) to zero. This yields either

$$\beta_0 = \gamma\delta = \left[\frac{B(\frac{7}{6},\frac{3}{2})}{2B(\frac{11}{6},\frac{1}{2})}\right]^{\frac{1}{2}} \approx 0.442\ldots \tag{16a}$$

or

$$\gamma^2\delta^2\left(2B(\tfrac{11}{6},\tfrac{1}{2}) - \frac{1}{3\gamma^3}B(\tfrac{17}{6},\tfrac{1}{2})\right) = B(\tfrac{7}{6},\tfrac{3}{2}), \tag{16b}$$

which corresponds to the curve β_1 on figure 14. As can be seen, the two curves are almost identical except for γ near 1, where the theory is not strictly valid in any event.

Apart from the two curves on figure 14, experimental and computer-simulation predictions of bubble migration are also indicated. Again it is found that the Kelvin impulse appears to determine the response behaviour of a bubble near a boundary, in this case a free surface.

5. Conclusions

In this paper we have considered the growth and collapse of a buoyant vapour bubble near a free surface. While a free surface repels the pulsating bubble through the Bjerknes effect, buoyancy forces act in the opposite direction and may induce the bubble to migrate towards the free surface. The Kelvin impulse of the bubble appears to yield the criterion that determines the bubble's motion. From these calculations it appears that $\gamma\delta \approx 0.442$ determines the null-impulse line which separates the parameter space determining the bubble's migratory behaviour.

The numerical simulations performed in the paper indicate that the nonlinear terms in the free-surface boundary condition become extremely important for $\gamma < 1.5$. The examples at $\gamma = 1.0$ and 0.98 (cf. experiment) clearly indicate this, with a high-speed free-surface jet ('spike') being formed even during the collapse phase. This leads to the phenomenon of a stagnation point appearing in the main body of fluid between the bubble and the free surface. A point of maximum pressure also occurs between the two surfaces, although it is at a different location to the stagnation point: a product of the unsteady fluid mechanics. The closer the bubble is to the free surface, the narrower the jet penetrating the bubble, a phenomenon noted in previous studies (Chahine 1977; Blake & Gibson 1981).

Buoyancy forces can reverse the direction of bubble migration provided $\gamma\delta > 0.442$, in which case the bubble moves towards the free surface. In these cases a relatively broad jet is formed, plunging through the bubble from underneath. While the free surface suffers a significant nonlinear deformation for small γ-values, it does not suffer the extreme deformations of the gravity-free case when the maximum pressure is between the bubble and free surface.

The motion of a cavitation bubble near a boundary depends on a number of factors: the distance from the boundary, the properties of the boundary and the ambient velocity and pressure fields. In Part 1 and this paper we have considered two types of boundaries (i.e. rigid boundary and free surface) whose properties result in opposite responses of the bubble: the rigid boundary attracts the bubble, the free surface repels it. Externally imposed flow effects can dramatically alter the behaviour of the bubble indicating that a thorough understanding of a cavitation-bubble dynamics will require full details of the lifetime dynamics of a bubble.

These two papers have provided us with several of the criteria that determine the motion of a cavitating bubble near a boundary together with a more detailed understanding of the small-scale physics near the bubble.

The financial support given by the Government of Malaysia and the Universiti Pertanian Malaysia to Bachok bin Taib during his graduate studies at the Univerity of Wollongong are gratefully acknowledged. The authors acknowledge the frequent comments and suggestions of Dr D. C. Gibson of the CSIRO Division of Energy Technology. Acknowledgement is also made of support from the Australian Research Grants Scheme.

REFERENCES

BLAKE, J. R. 1983 The Kelvin impulse: application to bubble dynamics. In *Proc. 8th Austral. Fluid Mech. Conf.*, vol. 2, pp. 10B.1–10B.4. Newcastle, Australia: Institution of Engineers.

BLAKE, J. R. & CERONE, P. 1982 A note on the impulse due to a vapour bubble near a boundary. *J. Austral. Math. Soc.* **B 23**, 383–393.

BLAKE, J. R., CERONE, P. & GIBSON, D. C. 1984 A note on the growth and collapse of buoyant vapour bubbles near a free surface. *Preprint No.* 9/84, Department of Mathematics, University of Wollongong.

BLAKE, J. R. & GIBSON, D. C. 1981 Growth and collapse of a vapour cavity near a free surface. *J. Fluid Mech.* **111**, 123–140.

BLAKE, J. R., TAIB, B. B. & DOHERTY, G. 1986 Transient cavities near boundaries. Part 1. Rigid boundary. *J. Fluid Mech.* **170**, 479–497.

CERONE, P. & BLAKE, J. R. 1984 A note on the instantaneous streamlines, pathlines and pressure contours for a cavitation bubble near a boundary. *J. Austral. Math. Soc.* **B 26**, 31–44.

CHAHINE, G. L. 1977 Interaction between an oscillating bubble and a free surface. *Trans. ASME* I: *J. Fluids Engng* **99**, 709–716.

CHAHINE, G. L. & BOVIS, A. 1980 Oscillation and collapse of a cavitation bubble in the vicinity of a two-liquid interface. In *Cavitation and Inhomogeneities in Underwater Acoustics* (ed. W. Lauterborn), pp. 23–29. Springer.

GIBSON, D. C. 1968 Cavitation adjacent to plane boundaries. In *Proc. 3rd Austral. Conf. on Hydraulics and Fluid Mech.*, pp. 210–214. Sydney, Australia: Institution of Engineers.

GIBSON, D. C. & BLAKE, J. R. 1980 Growth and collapse of cavitation bubbles near flexible boundaries. In *Proc. 7th Aust. Conf. on Hydraulics and Fluid Mech.*, pp. 283–286. Brisbane, Australia: Institution of Engineers.

GIBSON, D. C. & BLAKE, J. R. 1982 The growth and collapse of bubbles near deformable surfaces. *Appl. Sci. Res.* **9**, 215–224.

HOLT, M. 1977 Underwater explosions. *Ann. Rev. Fluid Mech.* **9**, 187–214.

LENOIR, M. 1976 Calcul numérique de d'implosion d'une bulle de cavitation au voisinage d'une paroi ou d'une surface libre. *J. Méc.* **15**, 725–751.

LONGUET-HIGGINS, M. S. & COKELET, E. D. 1976 The deformation of steep surface waves on water. 1. A numerical method of computation. *Proc. R. Soc. Lond.* A **350**, 1–26.

TAIB, B. B. 1985 Boundary integral methods applied to cavitation bubble dynamics. Ph.D. thesis, University of Wollongong.

TAIB, B. B., DOHERTY, G. & BLAKE, J. R. 1984 Boundary integral methods applied to cavitation bubble dynamics. In *Proc. Centre Math. Anal. Workshop* (ed. S. A. Gustafson & R. S. Womersley), vol. 6, pp. 166–186.